Cao *et al. Energy Mater* 2022;2:200010
DOI: 10.20517/energymater.2022.06

Energy Materials

Article

Open Access

Check for updates

Strained carbon steel as a highly efficient catalyst for seawater electrolysis

Xun Cao[1,#,*], Liyin Zhang[1,#], Kang Huang[2], Bowei Zhang[2], Junsheng Wu[2,*], Yizhong Huang[1,*]

[1]School of Materials Science and Engineering, Nanyang Technological University, 50 Nanyang Avenue, Singapore 639798, Singapore
[2]Institute for Advanced Materials and Technology, University of Science and Technology Beijing, 30 Xueyuan Road, Haidian District, Beijing 100083, China
[#]Authors contributed equally.

***Correspondence to:** Dr. Cao Xun, School of Materials Science and Engineering, Nanyang Technological University, 50 Nanyang Avenue, Singapore 639798, Singapore. E-mail: CAOX0015@e.ntu.edu.sg; Associate Professor Huang Yizhong, School of Materials Science and Engineering, Nanyang Technological University, 50 Nanyang Avenue, Singapore 639798, Singapore. E-mail: YZHuang@ntu.edu.sg; Professor Wu Junsheng, Institute for Advanced Materials and Technology, University of Science and Technology Beijing, 30 Xueyuan Road, Haidian District, Beijing 100083, China. E-mail: wujs@ustb.edu.cn; wujs76@163.com

How to cite this article: Cao X, Zhang L, Huang K, Zhang B, Wu J, Huang Y. Strained carbon steel as a highly efficient catalyst for seawater electrolysis. *Energy Mater* 2022;2:200010. https://dx.doi.org/10.20517/energymater.2022.06

Received: 27 Feb 2022 **First Decision:** 18 Mar 2022 **Revised:** 27 Mar 2022 **Accepted:** 1 Apr 2022 **Published:** 12 Apr 2022

Academic Editors: Yuping Wu, Bin Zhu **Copy Editor:** Tiantian Shi **Production Editor:** Tiantian Shi

Abstract

In response to the global energy crisis, water splitting has become one of the most efficient methods to produce hydrogen as an excellent substitute for fossil fuels. The diffusion coefficient of hydrogen and its interaction with iron have granted carbon steel (CS) the susceptible nature to hydrogen, and therefore CS is considered a promising electrocatalyst in the hydrogen evolution reaction. Compared to many traditional alkaline electrolytes, simulated seawater exhibits reasonable performance that facilitates an effective hydrogen evolution reaction. In the electrolysis of simulated seawater, the lowest overpotential of strained CS samples (-391.08 mV) is comparable to that of Pt plate electrodes (-377.31 mV). This is the result of the plane strain introduced to CS samples by a hydraulic press and indentation, which help to facilitate mass transport through diffusion for hydrogen evolution. The susceptibility of CS is verified by the formation of nanoscale hydrogen blisters that form in the proximity of grain boundaries. These blisters are the result of hydrogen gas pressure that is built up by the absorbed atomic hydrogen. These hydrogen atoms are believed to accumulate along the CS {1 1 0} planes adjacent to grain boundaries. CS has so far not been studied for the catalysis of water splitting. In this study, CS is used as an electrocatalyst for the first time as a cost-effective method for the utilization of seawater that further contributes to the promotion of green energy production.

Keywords: Hydrogen evolution reaction, carbon steel, seawater electrolysis, strain engineering, hydrogen blistering, surface energy

INTRODUCTION

The rapid increase in human activity since the mid-19th century has catalyzed the process of global warming. Our over-reliance on non-renewable energy sources, such as fossil fuels, has resulted in a detrimental side effect on the ecosystem of the Earth. There is therefore an urgent need to develop alternative energy sources that are renewable and have minimal impact on the planet, with common practices including the utilization of solar cells and fuel cells[1-8], as well as finding energy storage solutions[9-13]. Clean energy, such as hydrogen fuel, is a promising substitute for petroleum because of its advantages that include low to zero carbon emissions, an almost unlimited supply source, ease of operation and independence from foreign control[14]. While hydrogen itself is a form of green energy that produces little to no pollutants, the process of producing hydrogen is not necessarily clean.

Hydrogen gas only exists in the atmosphere with a tiny fraction, and thus most has to be extracted from its compounds, such as water or methane gas. There are three main methods for hydrogen production, namely, steam methane reforming (SMR), coal gasification (CG) and water splitting[15]. About 96% of the global hydrogen supply is obtained from SMR and CG[15], which are economically viable but not environmentally friendly. Although the cleaner method of producing hydrogen is by water splitting via the hydrogen evolution reaction (HER), this method is hindered by the high cost of the catalyst used in the chemical reaction process[16-21].

The state-of-the-art electrocatalysts for water splitting are primarily noble metals (NMs, particularly Pt-based alloys for the HER)[22-25] that are commonly used in industry; however, their high cost impedes the advancement of the economical production of hydrogen fuel. Thus, significant research has been focused on exploiting electrocatalyst materials as alternatives to NMs with comparable performance at a much lower cost. Several critical types of NM-free electrocatalysts have been widely studied, including hydroxides/oxides[26-32], chalcogenides[29,33-36], nitrides[37-41], carbides[40,42,43], phosphides[19,44] and the alloys of transition metals[45,46]. Recent research has been heavily focused on metal/alloy-based electrocatalysts[47-57]. The excellent performance of a catalyst for water splitting can generally be achieved by increasing its electrochemically active surface area, tuning its electronic structure or enhancing its hydrogen adsorption energy.

Whilst novel catalysts are currently being developed, many still include NMs, and their synthesis procedures are usually complicated and require expensive chemicals and/or equipment. These factors reveal the advantages of common engineering alloys based on traditional transition metals, such as stainless steel[58] and carbon steel (CS), with the latter having not been investigated in detail regarding its electrocatalytic HER activity. Gennero de Chialvo *et al.*[59] showed that a smooth iron rotating disc electrode has good temperature-dependent HER performance in a 2 M NaOH solution. Based on the Volmer-Heyrovsky-Tafel mechanism, hydrogen atoms can be easily adsorbed onto the surface of the iron electrode and then embodied into the metal, thereby representing strong theoretical support that CS is susceptible to hydrogen[60]. In order to utilize CS as a potential catalyst for the HER, the catastrophic failure caused by strong blistering[61-65] must be avoided. Another previous study demonstrated that hydrogen preferentially segregates at the interfacial regions in iron and iron-based materials, and its diffusion coefficient can be expressed as a function of temperature, with a value of ~7.1×10^{-10} m^2/s at 300 K and an activation barrier of 0.11 eV[66]. However, little research has been carried out to study the catalytic HER performance of CS in

various types of electrolytes and methods for possible improvement, because of the poor efficiency and large overpotential observed[67-69].

Seawater and CS are clearly highly abundant materials and, therefore, would represent an excellent economic approach if they could be utilized for water splitting. In this work, bulk polished CS samples are subjected to electrolytes of different pH values to evaluate their HER performance. A simple mechanical processing method is also introduced to enhance the HER performance of the samples in a simulated seawater electrolyte.

EXPERIMENTAL

The chemicals used in this work include sodium chloride (NaCl, reagent grade, Sigma-Aldrich) and potassium hydroxide (KOH, 90%, Sigma-Aldrich) flakes, which were used as received without any further purification. The deionized water used was generated from a Milli-Q system with $\rho = 18.2$ MΩ·cm.

Processing of samples

Bulk CS samples (10 × 10 × 3 mm^3) were mechanically polished with fine grit (P180) SiC paper using a polisher (Forcipol 300-IV, Kemet International Limited, UK) operated at a speed of 200 rpm under a constant water supply. They were then cut into thinner sections (10 × 10 × 1 mm^3) using a linear precision saw (IsoMet® 4000, Buehler, USA) equipped with a Series 20LC diamond blade operated at a feed rate of 1 mm/min and a blade speed of 4000 rpm. The thin samples were dried under a hot air flow. Mechanical deformation was carried out on the samples using a hydraulic press, and the load applied was 0-10 t at an interval of 2 t. These samples are hereafter denoted as CS-0t, CS-2t, CS-4t, CS-6t and CS-8, respectively. Indentations were carried out using a Rockwell hardness tester on the polished surface of the samples with a load of 60 kgf.

Characterization and testing techniques

The crystalline phases of the bulk samples were determined by X-ray diffraction (XRD) using a bulk X-ray diffractometer (XRD-6000, Shimadzu, Japan) with Cu-Kα radiation produced at 40 kV and 30 mA with $\lambda \approx 1.5405986$ Å. All samples were scanned within the range of $5° \leq 2\theta \leq 120°$ under θ-2θ mode at a speed of 1°/min. The morphologies of the samples were characterized using thermionic scanning electron microscopy (SEM, JSM-6360A, JEOL, Japan) with an accelerating voltage of 10 kV under secondary electron imaging mode. The elemental compositions of the samples were confirmed by X-ray energy-dispersive spectroscopy (XEDS) performed at an accelerating voltage of 20 kV with an XEDS attachment (JED-2300, JEOL, Japan) on the scanning electron microscope. The interfacial structures of the sample with the best performance before and after the HER test were examined using field-emission gun transmission electron microscopy (TEM, JEM-2100F, JEOL, Japan) operated at an accelerating voltage of 200 kV. The cross-sectional lamellae were prepared with an *in-situ* lift-out method using a dual-beam focused ion beam (FIB, XB540, Zeiss, Germany) system equipped with a tungsten needle (OMNIprobe 400, Oxford Instruments, UK).

The HER catalytic activities of the samples were tested on a three-electrode electrochemical workstation (PGSTAT302N, Metrohm Autolab, Netherlands). The CS samples, a Pt plate and an Ag/AgCl electrode were used as the working, counter and reference electrodes, respectively. An appropriate amount of KOH was dissolved in deionized water to form solutions of different concentrations, so the pH values of the electrolyte vary from 8 to 14. Appropriate amounts of NaCl and KOH were dissolved in deionized water to form a solution with a similar salinity to seawater (3.5% salt solution with pH 8), and the simulated seawater was used as the electrolyte for further testing. Linear sweep voltammetry (LSV) was carried out at a

scanning rate of 2 mV/s. To estimate the double-layer capacitance (C_{dl}) of the samples, cyclic voltammetry (CV) was conducted within a non-Faradaic potential range from -0.5 to -0.9 V with scanning rates varied from 10 to 100 mV/s. Electrochemical impedance spectroscopy (EIS) was carried out at a fixed working electrode current density of 10 mA/cm^2 with a frequency range of 10^5-10^{-2} Hz. Stability tests were conducted using chronopotentiometry (CP) held at a constant working electrode current density (WECD) of -10 mA/cm^2 for a continuous period of 12 h.

RESULTS AND DISCUSSION

Phase identification

Figure 1A shows the XRD patterns of the bulk samples before and after polishing. Most of the diffraction peaks could be ascribed to CS, which has a similar structure to body centered cubic (BCC) Fe (JCPDS No. 06-0696, space group *I*m-3m). Before polishing, the unprocessed sample has a thin oxide layer on its surface (as marked by * in the red profile of Figure 1A), which might hinder the charge transfer process because of its semiconducting nature. Mechanical polishing removes the oxide layer, and almost all diffraction planes were exposed to a greater extent (blue profile of Figure 1A).

Previous research has shown that for BCC Fe, the surface energy of the (2 1 1) plane is the largest and the (1 1 0) plane is the second largest[70]. However, the (1 1 0) plane is hypothesized to be the most favorable for the electrochemical HER, as the (1 1 0) plane of Fe has the largest Fe-H binding energy[71], which could promote the adsorption and desorption of hydrogen. The SEM images in Figures 1B and C illustrate the morphological differences before and after mechanical polishing. The oxide layer is comprised of small nanometer to micrometer-sized spherical particles with an uneven distribution [Figure 1B], whereas after mechanical polishing, the surface becomes much smoother with parallel scratches [Figure 1C], which should be formed along the direction of polishing.

Electrocatalytic performance for HER

The catalytic performance of the samples for the HER was evaluated by electrochemical tests. The bulk samples after polishing were first subjected to electrolytes of different pH values and LSV was performed from -0.6 to -1.5 V (*vs.* Ag/AgCl), as shown in Figure 2A. It could be observed that as the pH moves towards neutral, the electrochemical response weakens drastically. KOH electrolytes with pH < 13 cannot achieve a WECD of -10 mA/cm^2, even when reaching an applied potential of -1.5 V *vs.* Ag/AgCl. The trend line in Figure 2B reveals that the WECD has an exponential relationship with the anion concentration in the electrolyte, as evidenced by the perfect fitting. It is noteworthy that in the simulated seawater (pH 8 with 3.5% NaCl), which has an anion concentration of ~0.6 M, the sample produces a WECD of -11.15 mA/cm^2 and this value only slightly supersedes the KOH electrolyte with pH 12, which has an anion concentration of 10 mM. In addition to the limited amount of OH^- ions in the simulated seawater, the significant difference in the ionic concentrations also results in a much higher Cl^- ionic strength[72] that hinders the mass transport of OH^- ions[73], thereby lowering the turnover frequency of the oxygen evolution reaction and the chlorine evolution reaction (CER) takes over at the anode. Since Cl^- has much lower ion mobility compared to OH^-[74], the CER-dominated water splitting[75] performs weaker in terms of the WECD at -1.5 V.

The LSV curves of the samples are displayed in Figure 3A and the overpotentials (η_{10}) of the samples are recorded at a current density of -10 mA/cm^2. The smallest (-504.26 mV) comes from CS-8t and has an effective improvement compared to that of CS-0t (-758.16 mV). These values render a decreasing trend with a quadratic function [Figure 3B] and solving the derivative function confirms that the reduction in overpotential would cease upon reaching a pressure of ~11.5 t applied on the bulk sample. This limited

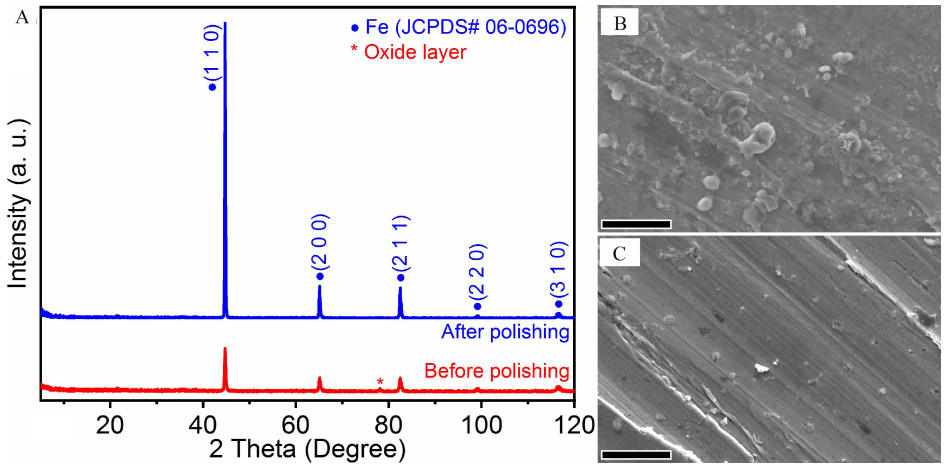

Figure 1. (A) XRD patterns of bulk samples before and after polishing. SEM images of bulk samples before (B) and after (C) polishing (scale bar: 5 μm).

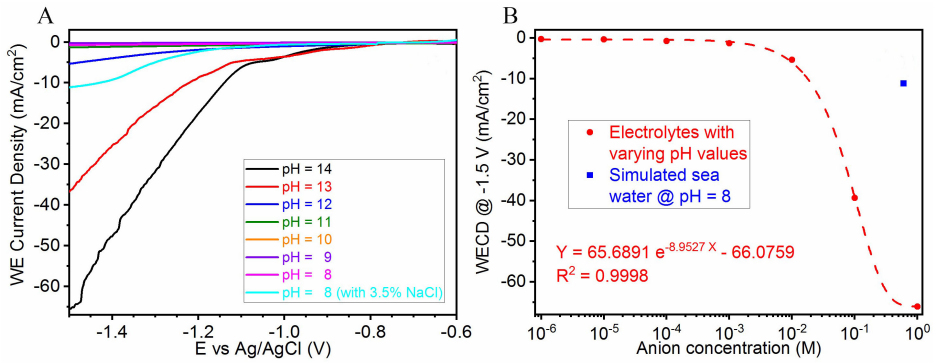

Figure 2. (A) LSV curves and (B) trend line in working electrode current densities of polished samples in electrolytes of different pH values.

reduction is believed to originate from the uniaxial strain resulting from the high pressure, which increases the total surface energy of the sample and lowers the activation energy of the entire process, thereby triggering better performance and higher efficiency in the overall catalysis. This is supported by the respective Tafel plots of the samples [Figure 3A], where the Tafel slope drops sharply from 1609 mV/dec (CS-0t) to 318 mV/dec (CS-2t) with externally applied pressure, indicating an enhancement in the catalytic performance. Further loading gives a much gentler decreasing trend and in overall, it follows a linear relationship between the natural logarithms of both the pressure loading and the Tafel slope [Figure 3B].

Figure 3C shows the galvanostatic EIS results, which confirm a relatively small solution resistance (R_s) for the simulated seawater electrolyte (< 10 Ω). As the pressure loading increases, the charge transfer resistance (R_{ct}) of the HER becomes slightly reduced and this is an accreditation of the increment in the surface energy of the CS samples, indicating a faster H^+ reduction charge transfer process[76] and thus higher Faradic efficiency is expected during the HER[77]. Furthermore, the CS-0t and CS-8t samples were subjected to CV tests with varying scanning rates in the non-Faradaic potential range [Figures 3E and F] and the working electrode current is plotted against the scanning rate. The gradient of the linear fit represents the double-layer capacitance (C_{dl}) of the samples, which gently increases [Figure 3D] from 11.6 mF (CS-0t) to 14.5 mF (CS-8t), in agreement with the EIS results according to the equivalent circuit diagram [Figure 3D]. With

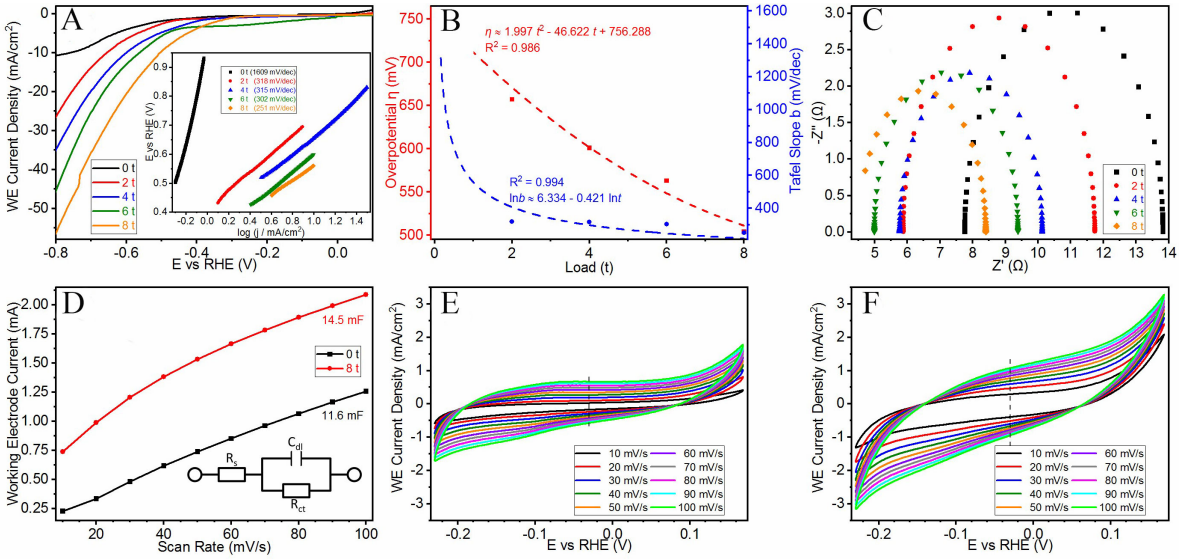

Figure 3. Electrochemical tests conducted on CS samples using simulated seawater. (A) LSV curves and (inset) Tafel plots. (B) Trend lines for changes in overpotentials and Tafel slopes. (C) Nyquist plots of all samples. (D) Calculated C_{dl} values based on CV curves of (E) CS-0t and (F) CS-8t and (inset) equivalent circuit diagram.

relatively constant and small R_s values, the gentle increase in C_{dl} and decrease in R_{ct} are not expected to affect the overall performance. However, there is an extra amount of energy equivalent to an 8t suppressing force applied to CS-8t and the incorporation of this large strain energy is believed to produce this performance improvement.

The ECSAs of the samples are directly proportional to their respective C_{dl} values. The ECSA of CS-0t and reference Pt plate is assumed to be 1 cm^2, and thus the ECSA of CS-8t (labelled as CS-0 in Table 1) is ~1.25 cm^2. To further improve the electrocatalytic performance, CS-8t samples were subjected to various numbers of indents, and the respective ECSA values are listed in Table 1. Each indent has a diagonal length of ~600 μm, as shown in the SEM image of Figure 4D. Through a comparison of the ECSA-normalized activities [Figure 4A][58,78], it is obvious that the bulk Pt plate still serves as the state-of-the-art catalyst in seawater electrolysis with a relatively small η_{10} of -377.31 mV. Nevertheless, indentation resulted in a significant enhancement in the CS-8t samples, with the smallest η_{10} of -391.08 mV achieved by making 16 indents, which is close to the performance of the bulk Pt plate. The enhancement is linearly correlated with the number of indents, as shown in the red profile of Figure 4B.

The TOF values were obtained at E = -1.377 V (*vs.* RHE), at which the Pt plate produces a current density of -10 mA/cm^2. As listed in Table 1, the Pt plate has the largest TOF value and that of CS-16 is very close to the Pt plate. The original CS-8t sample (CS-0 with no indent) has a much smaller TOF as it responds much slower to the HER process compared to other indented samples. This is likely because indentation could produce a large amount of active sites (along grain boundaries and hydrogen blisters, as shown in Figure 5). This also shows that indentation is the second major influencing factor after hydraulic press, and it also renders linear correlation to the TOF values (blue profile in Figure 4B).

From a comparison of the EIS results [Figure 4C], the CS-16 sample has similar R_s (5.87 *vs.* 4.38 Ω) and R_{ct} (~6 *vs.* ~5 Ω) values to the Pt plate, indicating that strain engineering is a good method to improve the performance of catalytic materials through the exposure of more active sites for charge transfer and the

Table 1. Electrochemically active surface area (ECSA) and turnover frequency (TOF) values of samples

Label	Sample	ECSA (cm^2)	TOF (s^{-1})
Pt plate	Pt plate	1.0000	34.0348
CS-0	CS-8t	1.2500	9.95842
CS-1	CS-8t with 1 indent	1.2536	23.7519
CS-4	CS-8t with 4 indents	1.2644	25.8727
CS-9	CS-8t with 9 indents	1.2824	28.7614
CS-16	**CS-8t with 16 indents**	**1.3076**	**31.6267**

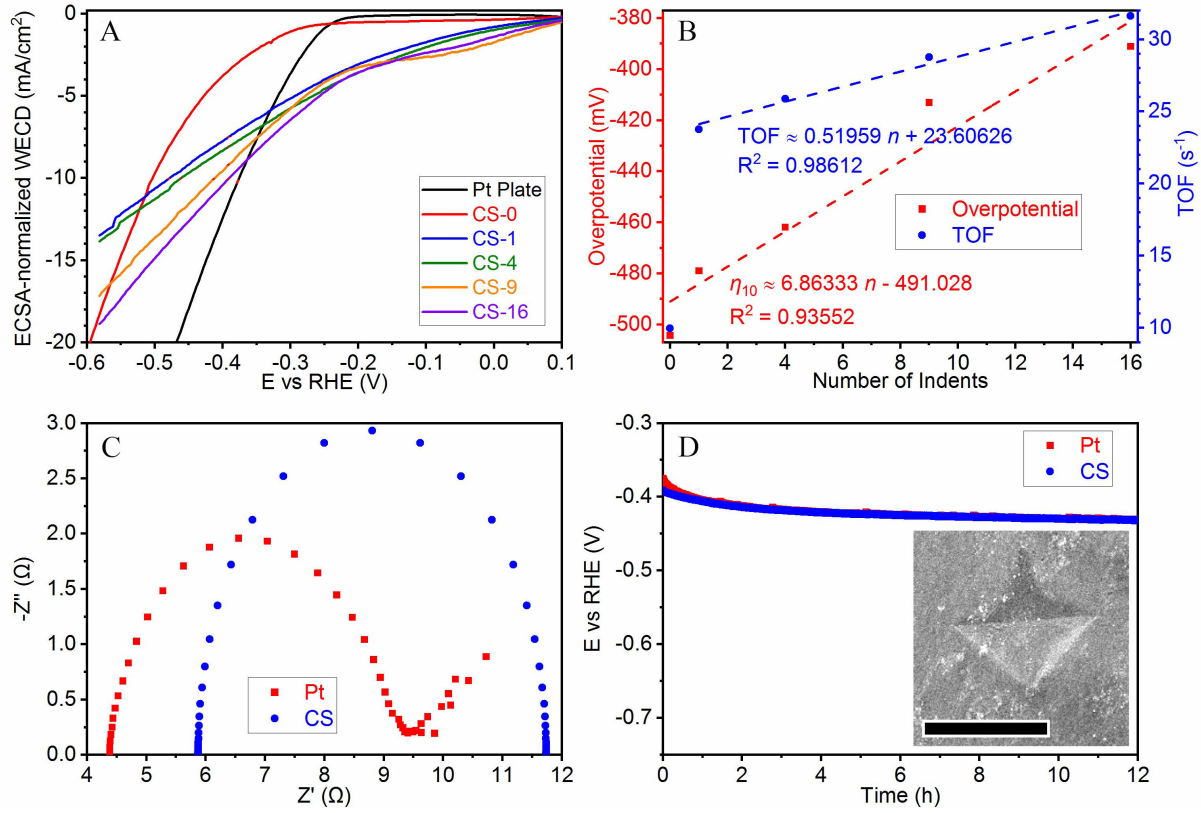

Figure 4. (A) LSV curves of Pt plate and CS-8t samples with various numbers of indents, showing their ECSA-normalized activities. (B) Linear fits of η_{10} and TOF values with number of indents. (C) Nyquist plots of Pt plate and CS-16 sample. (D) Stability tests of Pt plate and CS-16 sample using CP and (inset) SEM image of an indent (scale bar: 500 μm).

enlargement of interfacial density[79]. A 12-h stability test was also conducted for both the CS-16 sample and Pt plate using CP [Figure 4D]. Whilst holding at the constant WECD of -10 mA/cm², the stability of the CS-16 sample is comparable to the Pt plate and the change in η_{10} values is only ~30 mV over 12 h for both. The excellent stability of the CS-16 sample in the simulated seawater environment suggests that traditional CS materials under physical strain could be economic substitutes for Pt in the application of seawater electrolysis.

To characterize the formation of hydrogen blisters, cross-sectional lamellae were prepared from an indent on the CS-8t sample with 16 indents before and after the HER test [Figure 5]. Figure 5A shows a low-magnification TEM image of the CS sample before the HER test, where no hydrogen blisters are visible. A high-resolution TEM (HRTEM) image (of the white square region in Figure 5A) is displayed in Figure 5B,

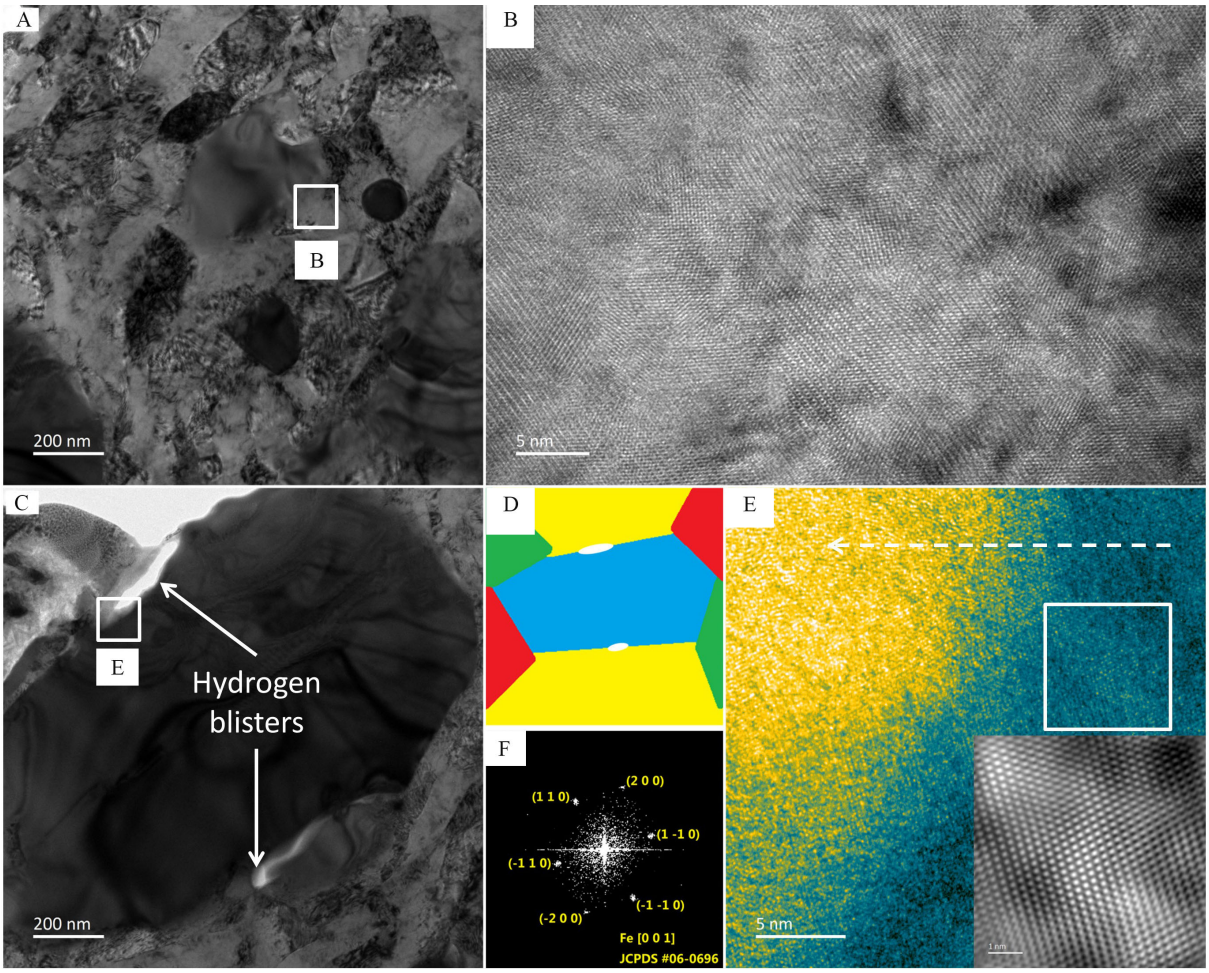

Figure 5. TEM characterizations of CS sample. (A) Low-magnification and (B) HRTEM images of CS sample before HER test. (C) Low-magnification and (E) HRTEM images of CS sample after HER test, where the white arrows indicate the hydrogen blisters formed. (D) A schematic diagram illustrating the position of the hydrogen blisters, which are formed at the grain boundaries. (F) FFT pattern transformed from the white square region in (E). The inset of (E) is an FFT image transformed from (F).

which shows the high crystallinity of the sample across the entire image. Hydrogen blisters (shown by the white arrows in Figure 5C) are formed during the HER process, which have a width of a few tens of nanometers and a lateral size of ~200 nm. Figure 5D presents a schematic illustration showing that the hydrogen blisters appear filiform in parallel with the sample surface and are formed in the proximity of the grain boundaries planar strained by the hydraulic press and indentation. The HRTEM image displayed in Figure 5E is taken from a region near a blister. A gradient could be identified along the white dashed arrow, which shows a gradual decrease in crystallinity. The region nearer to the blister (yellow color) became completely amorphous with no obvious lattice. The region further from the blister (blue color) has good crystallinity, as displayed by the clear lattice fringes [Figure 5E]. Part of the crystalline region appears dark and this should be due to the mass-thickness contrast as a result of the non-uniformity in the thickness of the lamella after FIB thinning.

The fast Fourier transform (FFT) pattern of the square region in Figure 5E is given in Figure 5F. By matching against the standard database using JEMS software (Electron Microscopy Software, Java Version 4.3905U2016, developed by Dr. P. Stadelmann, Switzerland), the sample was imaged along the zone axis of

(0 0 1) of BCC Fe and all diffractions indexed in the FFT pattern could be matched with the XRD pattern [Figure 1A]. The diffraction spots indicate that the longitudinal direction of the blister is perpendicular to the <1 1 0> direction, meaning that plane strain has been applied to the sample during hydraulic press and indentation and is accumulated in the {1 1 0} planes giving rise to large surface energy[70], which is in perfect agreement with the above hypothesis.

CONCLUSIONS

This work has systematically studied water splitting by CS samples using different electrolytes and possible methods to improve the electrocatalytic performance of CS in the HER were investigated. The working electrode current density could be expressed as an exponential function of the OH^- anion concentration in traditional alkaline electrolytes. The low ionic mobility of Cl^- in simulated seawater leads to weaker mass transport, but the HER performance is still in a reasonable range. A hydraulic press and microhardness indentation were employed to introduce plane stress to the CS samples, and the stress centers at the proximity of grain boundaries are where hydrogen blisters form during the HER to promote mass transport through diffusion. TEM characterization showed that the longitudinal side of the hydrogen blisters is perpendicular to the <1 1 0> direction of the crystal lattice, indicating that the applied stress/strain accumulated mostly in the {1 1 0} planes, which gives rise to the large surface energy. The overpotential η_{10} can be expressed as a quadratic function of the hydraulic press loading, which may reach a limit at ~11.5 t pressure, and a further improvement could be supported by indentation, which linearly affects the performance. In the electrolysis of simulated seawater, the strained CS sample could reach the lowest η_{10} of -391.08 mV and a small R_{ct} of 6 Ω, which are close to the Pt plate electrode. The synergistic effect of both straining methods successfully increased the surface energy and number of active sites on CS electrodes, which has been proven as an effective approach to improve the HER performance.

DECLARATIONS

Acknowledgments

This research was supported by the MOE AcRF Tier 1 grant RG79/20 (2020-T1-001-045). XRD, SEM, FIB and TEM characterizations were performed at the Facility for Analysis, Characterization, Testing and Simulation (FACTS) at Nanyang Technological University, Singapore. The authors would like to acknowledge the assistance provided by Ms. Han Yin and Ms. Tan Jia Wen Sarah on the sample preparation works.

Authors' contributions

Methodology, investigation, formal analysis, manuscript writing, visualization: Cao X, Zhang L
Validation, investigation: Huang K, Zhang B
Project administration, conceptualization, funding acquisition, supervision, manuscript revision: Wu J, Huang Y

Availability of data and materials

Not applicable.

Financial support and sponsorship

Not applicable.

Conflicts of interest

The authors declare that they have no conflict of interest.

Ethical approval and consent to participate

Not applicable.

Consent for publication

Not applicable.

REFERENCES

1. Cui P, Qu S, Zhang Q, et al. Perovskite homojunction solar cells: opportunities and challenges. *Energy Mater* 2021;1:100014. DOI
2. Yang M, Wei W, Zhou X, Wang Z, Duan C. Non-fused ring acceptors for organic solar cells. *Energy Mater* 2021;1:100008. DOI
3. Fan Q, Yan S, Wang H. Nanoscale redox reaction unlocking the next-generation low temperature fuel cell. *Energy Mater* 2022;2:200002. DOI
4. Lu Y, Zhu B, Shi J, Yun S. Advanced low-temperature solid oxide fuel cells based on a built-in electric field. *Energy Mater* 2021;1:100007. DOI
5. Zhu B, Mi Y, Xia C, et al. A nanoscale perspective on solid oxide and semiconductor membrane fuel cells: materials and technology. *Energy Mater* 2021;1:100002. DOI
6. Cao X, Li C, Lu Y, et al. Catalysis of Au nano-pyramids formed across the surfaces of ordered Au nano-ring arrays. *J Catal* 2019;377:389-99. DOI
7. Cao X, Li C, Peng D, et al. Highly strained au nanoparticles for improved electrocatalysis of ethanol oxidation reaction. *J Phys Chem Lett* 2020;11:3005-13. DOI PubMed
8. Cao X, Peng D, Wu C, et al. Flexible Au micro-array electrode with atomic-scale Au thin film for enhanced ethanol oxidation reaction. *Nano Res* 2021;14:311-9. DOI
9. He C, Cheng J, Liu Y, Zhang X, Wang B. Thin-walled hollow fibers for flexible high energy density fiber-shaped supercapacitors. *Energy Mater* 2021;1:100010. DOI
10. Castillo J, Qiao L, Santiago A, et al. Perspective of polymer-based solid-state Li-S batteries. *Energy Mater* 2022;2:200003. DOI
11. Huang T, Long M, Xiao JX, Liu H, Wang G. Recent research on emerging organic electrode materials for energy storage. *Energy Mater* 2021;1:100009. DOI
12. Chang H, Wu Y, Han X, Yi T. Recent developments in advanced anode materials for lithium-ion batteries. *Energy Mater* 2021;1:100003. DOI
13. Bashir T, Ismail SA, Song Y, et al. A review of the energy storage aspects of chemical elements for lithium-ion based batteries. *Energy Mater* 2021;1:100019. DOI
14. Hydrogen Fuel: Production, Transport, and Storage. 1st ed. 2008. DOI
15. Ogden JM. P Rospects For B Uilding A H Ydrogen E Nergy I Nfrastructure. *Annu Rev Energy Environ* 1999;24:227-79. DOI
16. Lin Y, Yuan G, Liu R, Zhou S, Sheehan SW, Wang D. Semiconductor nanostructure-based photoelectrochemical water splitting: A brief review. *Chem Phys Lett* 2011;507:209-15. DOI
17. Ahmad H, Kamarudin S, Minggu L, Kassim M. Hydrogen from photo-catalytic water splitting process: A review. Renew. . *Sust. Energ. Rev* 2015;43:599-610. DOI
18. Moniz SJA, Shevlin SA, Martin DJ, Guo Z, Tang J. Visible-light driven heterojunction photocatalysts for water splitting-a critical review. *Energy Environ Sci* 2015;8:731-59. DOI
19. Anantharaj S, Ede SR, Sakthikumar K, Karthick K, Mishra S, Kundu S. Recent trends and perspectives in electrochemical water splitting with an emphasis on sulfide, selenide, and phosphide catalysts of Fe, Co, and Ni: a review. *ACS Catal* 2016;6:8069-97. DOI
20. Yan Y, Xia BY, Zhao B, Wang X. A review on noble-metal-free bifunctional heterogeneous catalysts for overall electrochemical water splitting. *J Mater Chem A* 2016;4:17587-603. DOI
21. Joy J, Mathew J, George SC. Nanomaterials for photoelectrochemical water splitting-review. *Int. J. Hydrog* ;43:4804-17. DOI
22. Tavares M, Machado S, Mazo L. Study of hydrogen evolution reaction in acid medium on Pt microelectrodes. *Electrochimica Acta* 2001;46:4359-69. DOI
23. Skúlason E, Karlberg GS, Rossmeisl J, et al. Density functional theory calculations for the hydrogen evolution reaction in an electrochemical double layer on the Pt(111) electrode. *Phys Chem Chem Phys* 2007;9:3241-50. DOI PubMed
24. Grigoriev S, Millet P, Fateev V. Evaluation of carbon-supported Pt and Pd nanoparticles for the hydrogen evolution reaction in PEM water electrolysers. *J* ;177:281-5. DOI
25. Bai S, Wang C, Deng M, et al. Surface polarization matters: enhancing the hydrogen-evolution reaction by shrinking Pt shells in Pt-Pd-graphene stack structures. *Angew Chem Int Ed Engl* 2014;53:12120-4. DOI PubMed
26. Zhang B, Li C, Yang G, et al. Nanostructured CuO/C hollow shell@3D copper dendrites as a highly efficient electrocatalyst for oxygen evolution reaction. *ACS Appl Mater Interfaces* 2018;10:23807-12. DOI PubMed
27. Li C, Zhang B, Li Y, et al. Self-assembled Cu-Ni bimetal oxide 3D in-plane epitaxial structures for highly efficient oxygen evolution

reaction. *Appl. Catal. B* 2019;244:56-62. DOI

28. Ma M, Yang G, Wang H, et al. Ordered distributed nickel sulfide nanoparticles across graphite nanosheets for efficient oxygen evolution reaction electrocatalyst. *Int. J. Hydrog* ;44:1544-54. DOI
29. Peng D, Zhang B, Wu J, et al. Growth of lattice coherent Co_9S_8 /Co_3O_4 nano-heterostructure for maximizing the catalysis of co-based composites. *ChemCatChem* 2020;12:2431-5. DOI
30. Li C, Cao X, Li W, Zhang B, Xiao L. Co-synthesis of CuO-ZnO nanoflowers by low voltage liquid plasma discharge with brass electrode. J. Alloys. *Compd* 2019;773:762-9. DOI
31. Xiong T, Huang B, Wei J, et al. Unveiling the promotion of accelerated water dissociation kinetics on the hydrogen evolution catalysis of NiMoO4 nanorods. *J. Energy Chem* 2022;67:805-13. DOI
32. Yang F, Xiong T, Huang P, et al. Nanostructured transition metal compounds coated 3D porous core-shell carbon fiber as monolith water splitting electrocatalysts: a general strategy. *Chem. Eng. J* 2021;423:130279. DOI
33. Bonde J, Moses PG, Jaramillo TF, Nørskov JK, Chorkendorff I. Hydrogen evolution on nano-particulate transition metal sulfides. Faraday Discuss 2008;140:219-31; discussion 297-317. DOI PubMed
34. Zhao H, Zhang H, Cui G, et al. A photochemical synthesis route to typical transition metal sulfides as highly efficient cocatalyst for hydrogen evolution: from the case of NiS/g-C3N4. *Appl. Catal. B* 2018;225:284-90. DOI
35. Benck JD, Hellstern TR, Kibsgaard J, Chakthranont P, Jaramillo TF. Catalyzing the hydrogen evolution reaction (HER) with molybdenum sulfide nanomaterials. *ACS Catal* 2014;4:3957-71. DOI
36. Xu K, Wang F, Wang Z, et al. Component-controllable WS(2(1-x))Se(2x) nanotubes for efficient hydrogen evolution reaction. *ACS Nano* 2014;8:8468-76. DOI PubMed
37. Abghoui Y, Skúlason E. Hydrogen evolution reaction catalyzed by transition-metal nitrides. *J Phys Chem C* 2017;121:24036-45. DOI
38. Yu L, Song S, Mcelhenny B, et al. A universal synthesis strategy to make metal nitride electrocatalysts for hydrogen evolution reaction. *J Mater Chem A* 2019;7:19728-32. DOI
39. Theerthagiri J, Lee SJ, Murthy AP, Madhavan J, Choi MY. Fundamental aspects and recent advances in transition metal nitrides as electrocatalysts for hydrogen evolution reaction: A review. *Curr Opin* ;24:100805. DOI
40. Chen WF, Muckerman JT, Fujita E. Recent developments in transition metal carbides and nitrides as hydrogen evolution electrocatalysts. *Chem Commun (Camb)* 2013;49:8896-909. DOI PubMed
41. Xiong T, Yao X, Zhu Z, et al. In Situ grown co-based interstitial compounds: non-3d metal and non-metal dual modulation boosts alkaline and acidic hydrogen electrocatalysis. *Small* 2022;18:e2105331. DOI PubMed
42. Kim SK, Qiu Y, Zhang Y, Hurt R, Peterson A. Nanocomposites of transition-metal carbides on reduced graphite oxide as catalysts for the hydrogen evolution reaction. *Appl. Catal. B* 2018;235:36-44. DOI
43. Meyer S, Nikiforov AV, Petrushina IM, et al. Transition metal carbides (WC, Mo2C, TaC, NbC) as potential electrocatalysts for the hydrogen evolution reaction (HER) at medium temperatures. *Int. J. Hydrog. Energy* 2015;40:2905-11. DOI
44. Zhao X, Zhang Z, Cao X, et al. Elucidating the sources of activity and stability of FeP electrocatalyst for hydrogen evolution reactions in acidic and alkaline media. *Appl. Catal. B* 2020;260:118156. DOI
45. Huang K, Zhang B, Wu J, et al. Exploring the impact of atomic lattice deformation on oxygen evolution reactions based on a sub-5 nm pure face-centred cubic high-entropy alloy electrocatalyst. *J Mater Chem A* 2020;8:11938-47. DOI
46. Zhang Y, Xia X, Cao X, et al. Ultrafine metal nanoparticles/n-doped porous carbon hybrids coated on carbon fibers as flexible and binder-free water splitting catalysts. *Adv Energy Mater* 2017;7:1700220. DOI
47. Li C, Liu S, Jin X, et al. One-step fabrication of Cu2O-Cu catalytic electrodes with regular porous array by ultra-fast laser scanning. *J. Alloys Compd* 2022;900:163455. DOI
48. Chang S, Zhang Y, Zhang B, et al. Conductivity modulation of 3D-printed shellular electrodes through embedding nanocrystalline intermetallics into amorphous matrix for ultrahigh-current oxygen evolution. *Adv Energy Mater* 2021;11:2100968. DOI
49. Lu Y, Huang K, Cao X, et al. Atomically dispersed intrinsic hollow sites of. *M* :
M = Fe, Co, Ni, Cu, Pt, Ir) on FeCoNiCuPtIr nanocrystals enabling rapid water redox. Adv Funct Materials. DOI
50. Yang C, Gao N, Wang X, et al. Stable and efficient seawater splitting on a porous phosphate-intercalated NiFe (oxy)hydroxide@NiMoO4 core-shell micropillar electrode. *Energy Mater* 2021;1:100015. DOI
51. Llorente V, Diaz LA, Lacconi GI, Abuin GC, Franceschini EA. Effect of duty cycle on NiMo alloys prepared by pulsed electrodeposition for hydrogen evolution reaction. *J. Alloys Compd* 2022;897:163161. DOI
52. Cai C, Liu K, Zhu Y, et al. Optimizing hydrogen binding on Ru Sites with RuCo alloy nanosheets for efficient alkaline hydrogen evolution. *Angew Chem Int Ed Engl* 2022;61:e202113664. DOI PubMed
53. Feng D, Dong Y, Nie P, Zhang L, Qiao Z. CoNiCuMgZn high entropy alloy nanoparticles embedded onto graphene sheets via anchoring and alloying strategy as efficient electrocatalysts for hydrogen evolution reaction. *Chem. Eng. J* 2022;430:132883. DOI
54. Gao D, Guo J, He H, Xiao P, Zhang Y. Geometric and electronic modulation of fcc NiCo alloy by Group-VI B metal doping to accelerate hydrogen evolution reaction in acidic and alkaline media. *Chem. Eng. J* 2022;430:133110. DOI
55. Li C, Zhang L, Zhang Y, et al. PtRu alloy nanoparticles embedded on C2N nanosheets for efficient hydrogen evolution reaction in both acidic and alkaline solutions. *Chem. Eng. J* 2022;428:131085. DOI
56. Ma S, Deng J, Xu Y, et al. Pollen-like self-supported FeIr alloy for improved hydrogen evolution reaction in acid electrolyte. *J. Energy Chem* 2022;66:560-5. DOI
57. Pang B, Liu X, Liu T, et al. Laser-assisted high-performance PtRu alloy for pH-universal hydrogen evolution. *Energy Environ Sci*

2022;15:102-8. DOI

58. Gao Y, Xiong T, Li Y, Huang Y, Li Y, Balogun MJT. A simple and scalable approach to remarkably boost the overall water splitting activity of stainless steel electrocatalysts. *ACS Omega* 2019;4:16130-8. DOI PubMed PMC
59. de Chialvo MR, Chialvo AC. Hydrogen evolution reaction on a smooth iron electrode in alkaline solution at different temperatures. *Phys Chem Chem Phys* ;3:3180-4. DOI
60. Khodir S, Morisada Y, Fujii H. Suppression of hydrogen-induced blisters in SK4 carbon steel alloy by friction stir processing. *J Mater Sci* 2013;48:4313-20. DOI
61. Griesche A, Dabah E, Kannengiesser T, Kardjilov N, Hilger A, Manke I. Three-dimensional imaging of hydrogen blister in iron with neutron tomography. *Acta Materialia* 2014;78:14-22. DOI
62. Sun Y, Fujii H, Imai H, Kondoh K. Suppression of hydrogen-induced damage in friction stir welded low carbon steel joints. *Corrosion Science* 2015;94:88-98. DOI
63. Eliezer D. High-temperature hydrogen attack of carbon steel. *J Mater Sci* 1981;16:2962-6. DOI
64. Wasim M, Djukic MB. Hydrogen embrittlement of low carbon structural steel at macro-, micro- and nano-levels. *Int. J. Hydrog. Energy* 2020;45:2145-56. DOI
65. Ju C, Rigsbee J. The role of microstructure for hydrogen-induced blistering and stepwise cracking in a plain medium carbon steel. *Materials Science and Engineering* 1985;74:47-53. DOI
66. Islam MM, Zou C, van Duin AC, Raman S. Interactions of hydrogen with the iron and iron carbide interfaces: a ReaxFF molecular dynamics study. *Phys Chem Chem Phys* 2016;18:761-71. DOI PubMed
67. Lou X, Singh PM. Cathodic activities of oxygen and hydrogen on carbon steel in simulated fuel-grade ethanol. *Electrochimica Acta* 2011;56:2312-20. DOI
68. Safizadeh F, Ghali E, Houlachi G. Electrocatalysis developments for hydrogen evolution reaction in alkaline solutions-a Review. *Int. J. Hydrog. Energy* 2015;40:256-74. DOI
69. Elmeligi A, Ismail N. Hydrogen evolution reaction of low carbon steel electrode in hydrochloric acid as a source for hydrogen production. *Int. J. Hydrog. Energy* 2009;34:91-7. DOI
70. Vitos L, Ruban A, Skriver H, Kollár J. The surface energy of metals. *Surf Sci* 1998;411:186-202. DOI
71. Yule LC, Shkirskiy V, Aarons J, et al. Nanoscale active sites for the hydrogen evolution reaction on low carbon steel. *J Phys Chem C* 2019;123:24146-55. DOI
72. Amikam G, Nativ P, Gendel Y. Chlorine-free alkaline seawater electrolysis for hydrogen production. *Int. J. Hydrog. Energy* 2018;43:6504-14. DOI
73. Wintrich D, Öhl D, Barwe S, et al. Enhancing the selectivity between oxygen and chlorine towards chlorine during the anodic chlorine evolution reaction on a dimensionally stable anode. *Chem Electro Chem* 2019;6:3108-12. DOI
74. Duso AB, Chen DD. Proton and hydroxide ion mobility in capillary electrophoresis. *Anal Chem* 2002;74:2938-42. DOI PubMed
75. Dresp S, Dionigi F, Klingenhof M, Strasser P. Direct electrolytic splitting of seawater: opportunities and challenges. *ACS Energy Lett* 2019;4:933-42. DOI
76. Guo M, Qu Y, Yuan C, Chen S. Electrochemically assisted synthesis of three-dimensional FeP nanosheets to achieve high electrocatalytic activity for hydrogen evolution reaction. *Int. J. Hydrog. Energy* 2019;44:24197-208. DOI
77. Long X, Li G, Wang Z, et al. Metallic iron-nickel sulfide ultrathin nanosheets as a highly active electrocatalyst for hydrogen evolution reaction in acidic media. *J Am Chem Soc* 2015;137:11900-3. DOI PubMed
78. Zhang C, Shi Y, Yu Y, Du Y, Zhang B. Engineering sulfur defects, atomic thickness, and porous structures into cobalt sulfide nanosheets for efficient electrocatalytic alkaline hydrogen evolution. *ACS Catal* 2018;8:8077-83. DOI
79. Wei J, Zhou M, Long A, et al. Heterostructured electrocatalysts for hydrogen evolution reaction under alkaline conditions. *Nanomicro Lett* 2018;10:75. DOI PubMed PMC